SINERGI Vol. 30, No. 3, October 2026: 717-730
http://publikasi.mercubuana.ac.id/index.php/sinergi
http://doi.org/10.22441/sinergi.2026.3.004

Statistically validated comparative evaluation of fiducial markers for vision-based UAV precision landing in standardized PX4–ROS simulation

Anan Nugroho[1], Muhammad Ghulamzaki[1], Feddy Setio Pribadi[1], Khoirudin Fathoni[1], Dhidik Prastiyanto[1]*, Mona Subagja[2], Raihan Fa'iq Mubarak[1]
[1]Department of Electrical Engineering, Faculty of Engineering, Universitas Negeri Semarang, Indonesia
[2]Directorate of Information Systems and Public Relations, Universitas Negeri Semarang, Indonesia

Abstract
UAV quadcopter technology has advanced rapidly and is widely used in both military and civilian sectors. One critical challenge is precision landing, since conventional GPS-based methods have limited accuracy (0.9–1.8 m). Fiducial marker–based landing offers a practical alternative, but cross-study comparisons remain difficult because marker types and testing procedures vary. This study presents a statistically validated comparative evaluation of five fiducial markers (ArUco, AprilTag, ARTag, WhyCode, and STag) in a standardized PX4–ROS simulation environment. Beyond performance ranking, the study analyzes how marker geometry and coding structure influence homography stability, pose-estimation noise, and landing control response. Evaluation metrics include horizontal and vertical landing errors, landing time, and detection distance, analyzed using one-way ANOVA and Tukey HSD tests. Results show significant differences in vertical error, landing time, and detection distance, indicating that geometric regularity and edge-contrast structure directly affect visual pose stability. Within the controlled simulation framework, AprilTag shows the most consistent overall performance, with mean errors of 2.99 cm (X-axis) and 5.59 cm (Y-axis) and an average landing time of 21.8 s. The main contribution is a reproducible comparative framework and an explanatory link between marker design and visual-control stability, guiding marker selection in precision UAV landing systems.

Keywords:
Comparative;
Fiducial Marker;
Precision Landing;
Quadcopter;
Simulation;
UAV;

Article History:
Received: July 8, 2025
Revised: Decemeber 30, 2025
Accepted: February 20, 2026
Published: October 2, 2026

Corresponding Author:
Dhidik Prastiyanto
Department of Electrical Engineering, Faculty of Engineering, Universitas Negeri Semarang, Indonesia
Email:
dhidik.prastiyanto@mail.unnes.ac.id.

INTRODUCTION

A UAV quadcopter is an unmanned aerial vehicle with four motors that enables vertical takeoff and landing. It is widely utilized in both military and civilian sectors [1]. One of the main challenges in UAV operations is the landing system, which requires both high precision and reliability [2][3]. A landing failure can lead to significant losses in mission objectives and business assets [4]. While most UAVs rely on GPS for landing, conventional GPS systems have relatively low accuracy [5], with errors averaging 0.910 m [6], 1-2 meters [7], and 1.8 meters [8]. Precision landing is therefore crucial for applications such as mapping, package delivery [9], and autonomous recharging [10], as it helps mitigate risks such as cargo loss, equipment damage, and positioning errors, improving operational efficiency and success in complex environments.

Several methods have been developed to enhance precision landing, including GPS RTK (Real-Time Kinematic) [11][12], SLAM (Simultaneous Localization and Mapping) [13][14], Deep Learning-Based Vision [15][16], and Fiducial Markers [17][18].

Table 1. Comparison of Precision Landing Methods for UAV

Method	Description	Application
GPS RTK [11], [12]	Provides high accuracy with real-time corrections and works well in open areas, but has limited range and high cost because it requires a GPS reference station.	Ideal for outdoor applications such as precision mapping and crop spraying in large areas with stable GPS signals.
SLAM [13][14]	Uses LiDAR and camera sensors for mapping and positioning in unstructured environments. High cost due to the need for advanced hardware and complex processing.	Ideal for indoor environments or complex areas such as factories or buildings where external markers cannot be used.
Deep Learning-Based Vision [15][16]	Uses deep learning to detect objects and is effective in dynamic environments. High cost due to heavy computation and the need for large amounts of training data.	Ideal for complex applications involving moving objects, such as landing on vehicles or package delivery in dynamic settings.
Fiducial Markers [17][18]	Uses easily detected visual markers for position estimation, offering high accuracy and low cost with minimal computation.	Ideal for mapping and package delivery in open areas with pre-established markers and designated landing sites.

Table 1 shows that precision landing performance strongly depends on the chosen supporting method and its operational constraints. For the dominant use case, mapping and package delivery, a landing aid must deliver high positional accuracy with stable real-time performance under outdoor conditions [19,20,21]. In this context, fiducial marker–based landing provides the most suitable characteristics because it offers high precision, low computational load, low cost, and immunity to magnetic signal interference [22]. Consequently, fiducial marker systems have become a widely adopted visual-based approach for reliable pose estimation in precision landing [23]. Their effectiveness comes from the markers' distinct visual features, which enable accurate estimation of the camera's position and orientation, making pose estimation a direct and practical mechanism to support precision landing tasks [24].

The most popular fiducial markers for precision landing applications include AprilTag, ARTag, ArUco, STag, and WhyCode [25, 26, 27]. Table 2 summarizes and compares these markers.

Table 2 shows that the fiducial marker type affects precision landing performance. Although fiducial marker–based landing is more accurate than conventional GPS-based methods [28], marker performance depends on several key aspects, namely marker type and size [29]. Fiducial markers come in various types, which can make it difficult for new users to determine which type best suits their needs, thereby creating uncertainty in marker selection [30]. Selecting the appropriate marker is crucial because an incorrect choice can degrade landing performance [31]. Marker size also influences detection range and landing precision [29]. Differences in marker type, size, and testing conditions make objective comparative studies difficult, creating a research gap in selecting the best marker for precision landing.

To address this gap, this study offers novelty through a comparative analysis of five popular fiducial markers using a Kalman filter–based position estimation algorithm. All markers were tested with standardized sizes and procedures in simulation using a PX4 SITL–based quadcopter UAV in the Gazebo environment [19] [38], yielding consistent and objective comparative data to identify the best marker for precision landing. This research establishes a standardized simulation framework to ensure objective and reproducible evaluation.

Table 2. Comparison of Popular Fiducial Markers

Fiducial Marker	Description
ArUco [32]	ArUco-based precision landing with a size of 4x4 achieved an average precision landing of -34.1 cm.
AprilTag [33]	AprilTag-based precision landing with a size of 39 cm detected at a height of 0.7-4.5 m achieved an average outdoor precision landing of 9.35 cm from an altitude of 3 m.
ARTag [34]	The ARTag fiducial marker is designed to calculate the camera's position and orientation relative to world coordinates with high accuracy, making it a reliable alternative in environments with low GPS accuracy or no signal.
STag [35]	The STag fiducial marker enables stable pose estimation, minimizes estimation variability, and provides high stability in precision landing applications.
AprilTag 48h12 dan WhyCode Ellips [36]	Precision landing based on AprilTag 48h12 achieved an average precision landing of 8-9 cm and WhyCode Ellips 12-13 cm, with both markers detected at a height of less than 4 m.
ArUco [37]	ArUco precision landing with a size of 56x56 cm, detected at a maximum height of 30 m, achieved an average precision landing of 11 cm.

The framework integrates Gazebo, PX4 SITL, and ROS Noetic to create a controlled virtual environment in which five fiducial markers are tested under identical conditions [39] [40]. Each marker's performance is assessed using quantitative parameters, including landing accuracy on both the horizontal and vertical axes, landing time, and detection distance. We used one-way ANOVA and Tukey's HSD test to determine whether performance differences among markers were statistically significant. This methodological structure enables a fair and data-driven comparison, providing measurable insights into marker performance and serving as a foundation for identifying the most effective marker type for UAV precision landing.

METHOD

Material

Figure 1 illustrates the overall workflow of the visual-based autonomous landing system for UAV. The process begins by acquiring an input image from the onboard camera. The feature-based detector processes the captured frame to identify key points or patterns corresponding to the predefined fiducial marker. The corner detection module determines the marker's vertices to localize it accurately within the image. Next, the observation computation module calculates the marker's geometric parameters, including width, height, centroid position, and orientation. Finally, the platform tracking process utilizes these parameters to estimate the relative position between the UAV and the landing pad, enabling stable alignment for autonomous landing.

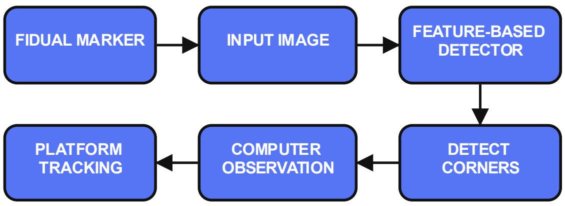

Figure 1. Block Diagram of Research Design

Simulation and Gazebo Environment

This study conducted a comparative analysis of five types of fiducial markers, namely ArUco, AprilTag, ARTag, STag, and WhyCode, to support the precision landing of quadcopter UAVs through integrated simulation. The simulation environment was built using Gazebo as the physics simulator, PX4 SITL as the virtual flight firmware, and ROS Noetic as the communication framework, managing image processing and pose estimation through MAVROS. Integrating these three platforms enables controlled, efficient testing without risk of hardware damage, while providing consistent evaluation scenarios to analyze detection stability and algorithmic performance for each marker type in the context of precision landing.

The UAV model used is an F450 quadcopter with an X configuration, a diagonal length of 450 mm, and a downward-facing virtual camera to detect markers during the landing phase, as shown in Figure 3. The Gazebo environment was configured with standard Earth gravity (-9.8 m/s²), a timestep of 0.004 seconds, and a real-time update rate of 250 Hz, using a flat grass field. A 30 × 30 cm square marker was placed with a position offset of 100 cm on the x and y axes (distance 141.42 cm) to simulate common GPS errors, as shown in Figure 2. This configuration ensures that the evaluation process reflects realistic operational conditions for UAVs during precision landing maneuvers.

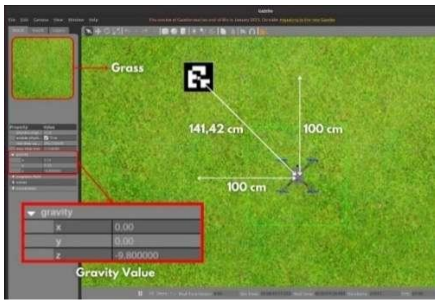

Figure 2. Gazebo Environment

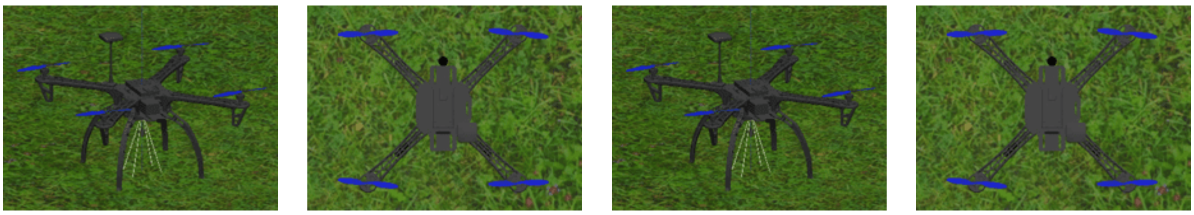

(a) (b) (c) (d)

Figure 3. UAV Quadcopter F450 Model (a) Side View (b) Top View (c) Left Side View (d) Front View

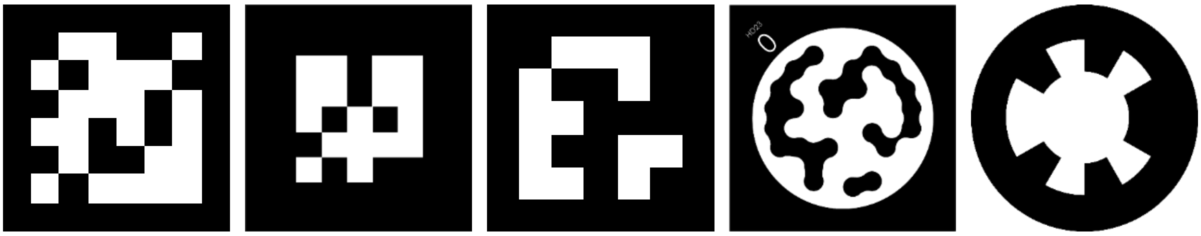

(a) (b) (c) (d) (e)

Figure 4. Fiducial markers: (a) AprilTag, (b) ARTag, (c) ArUco, (d) STag, (e) WhyCode

Fiducial Marker

Figure 4 shows five fiducial marker types tested: AprilTag, ARTag, ArUco, STag, and WhyCode. Each marker has unique characteristics and is detected using feature-based algorithms implemented with OpenCV.

AprilTag is known for its stability and detection accuracy, even at long distances. This marker utilizes a binary code with an optimized grid layout to minimize detection errors. Its detection pipeline extracts edges, identifies quadrilateral candidates, and robustly decodes the embedded bit pattern. By geometrically transforming the detected corner coordinates, the system provides high-precision positional information in real time, even in dynamic environments. Due to its reliable performance, AprilTag is widely used in robotics and UAV navigation applications, where it can accurately detect assembly target locations [41].

ARTag is designed for augmented reality and robot navigation, enabling high-accuracy estimation of a camera's position and orientation relative to the world coordinate system. ARTag uses binary patterns with error-correction mechanisms, ensuring reliable decoding under various noise conditions. After the marker corners are detected, the system projects their coordinates into three-dimensional space through perspective transformation, allowing it to compute the camera pose without external references. One of ARTag's main advantages is its capability to replace GPS-based algorithms when GPS signals are unavailable, enabling precise relative localization based on characteristic marker points [34]

ArUco is a binary code–based marker featuring a simple grid structure designed for efficient detection under varying illumination. Its detection process relies on adaptive thresholding to ensure robust segmentation, followed by verification of the internal binary code and pose calculation using the Perspective-n-Point (PnP) method. A key advantage of ArUco is its ability to detect markers even when they are partially occluded, while also offering flexibility in marker size and supporting unique identifiers for object recognition. This versatility makes ArUco suitable for a wide range of applications [23].

STag is a fiducial marker system that ensures stable and accurate pose estimation by incorporating precise geometric constraints. Its processing pipeline emphasizes edge refinement and contour consistency, significantly reducing pose variability and noise sensitivity. This stability makes STag particularly suitable for complex environments that demand high precision, such as multi-AGV (Automated Guided Vehicle) systems in smart warehouses, where reliable pose estimation is critical [35].

WhyCode enhances the WhyCon system by adding the ability to detect unique fiducial markers through rotation-invariant Binary Necklace patterns. The marker identification process involves cyclic matching of the bit sequence and segmentation-based estimation of the marker's center. These features allow WhyCode to maintain consistent readability regardless of orientation while providing computationally efficient position and orientation estimation. Implemented within a ROS-based framework, WhyCode offers a low-cost yet effective solution for robot tracking, including position, orientation, and velocity estimation, making it especially useful for affordable robotic testing platforms [42].

Modeling Feature-Based Detection

Object detection represents a fundamental component of robotic perception. In this study, we employ a feature-based detection approach because it efficiently identifies distinctive visual characteristics in an image. These detectors and descriptors are widely used because they quickly extract key points and patterns that inform recognition tasks. To ensure robustness, the extracted features should remain consistent despite changes in image rotation, scale, or affine transformations across multiple frames. In this study, we selected a SIFT-based feature extraction approach because it is robust to illumination changes, rotation, and scale variation, enabling consistent marker recognition under dynamic simulated lighting and camera perspectives [43].

In the detection process, we denote a set of feature points from the fiducial marker as $F_T \in \mathbb{R}^n$. At the same time, those from the current frame are represented as $F_S \in \mathbb{R}^m$, where $n$and $m$refer to the total number of features detected in each image. Each feature point in both the template and scene images is associated with a descriptor vector, defined as $D_T \in \mathbb{R}^{n\times k}$and $D_S \in \mathbb{R}^{m\times k}$, with k indicating the dimension of each descriptor. To determine correspondences between the two sets of images, the Euclidean distance between descriptors is calculated using (1):

$$d_{di} = \min \sum_{i=1}^{n} \sum_{j=1}^{m} \sqrt{(D_T(i,k))^2 - (D_s(j,k))^2} \quad (1)$$

Feature pairs with the smallest distance values are considered matching points. Consequently, a feature coordinate (x_i, y_i) in the template image corresponds to (x_i', y_i') in the captured scene frame, forming the foundation for the homography transformation used in the subsequent stage.

Homography and Corner Detection

After identifying feature correspondences between the template and the current image frame, a homography transformation maps the marker's coordinates from one plane to another. The homography matrix, denoted as $H \in \mathbb{R}^{3\times 3}$, establishes a projective relationship between the reference points in the template image and their corresponding points in the scene image. This relationship enables estimation of the marker's position, orientation, and scale within the image space, even when the camera viewpoint changes. Mathematically, the transformation can be expressed as shown in (2):

$$\begin{bmatrix} x^1 \\ y^1 \\ 1 \end{bmatrix} = H \begin{bmatrix} x \\ y \\ 1 \end{bmatrix} = \begin{bmatrix} h_{11} & h_{12} & h_{13} \\ h_{21} & h_{22} & h_{23} \\ h_{31} & h_{32} & h_{33} \end{bmatrix} \begin{bmatrix} x \\ y \\ 1 \end{bmatrix} \quad (2)$$

Here, (x, y) represents the coordinates of a feature point in the template image, while (x', y') denotes the transformed coordinates in the current image. The elements of H correspond to the coefficients that describe translation, rotation, scaling, and perspective distortion between the two planes.

Once the homography matrix is estimated, it can be used to identify the corner points of the fiducial marker. These corners provide the geometric reference necessary to compute the marker's centroid and its orientation relative to the camera frame. The centroid position serves as the basis for the subsequent observation computation process, allowing the system to determine the relative displacement and angular offset between the UAV and the landing target.

Observation Computation

The observation stage translates the geometric information from marker detection into measurable parameters that describe the UAV's relative position with respect to the landing platform. These observations are essential for estimating the system state and ensuring the UAV can align accurately during landing.

Based on the detected fiducial marker, several parameters are computed, including the centroid coordinates, the width and height of the detected area, and the orientation angle of the marker. These parameters are grouped into an observation vector Z_t using (3):

$$Z_t = \left[P_{ct}^{(i=5)}, O_w, O_h, \theta\right] \quad (3)$$

Where $P_{ct}^{(i=5)}$represents the centroid position of the detected marker in the image frame, $O_w$and $O_h$correspond to the width and height of the bounding box around the marker, and θindicates the rotation angle of the marker relative to the x-axis.

The centroid is calculated as the mean coordinate of all corner points identified during the homography stage. The width and height describe the marker's scale in the image, which can vary with the UAV's altitude and camera perspective. Meanwhile, the rotation angle θprovides orientation feedback that allows the control system to correct yaw misalignment during descent.

Together, these observations form the input vector for the state estimation process, serving as real-time visual feedback to the navigation and control system. Through this information, the UAV maintains stable alignment toward the landing pad even under disturbances or partial visual occlusions.

Kalman Filter

The Kalman filter is utilized as an estimator that infers hidden states from indirect and uncertain visual observations. It enables the system to process noisy data obtained from the detection module and generate a continuous estimate of the template position at each time step t.

We assume a linear dynamic system for the landing platform, where x_t and y_t denote the pixel coordinates of the marker's centroid at index t, and Δt is the time interval between consecutive image frames. The following discrete equations describe the temporal behavior of the position:

$$x_t = x_{t-1} + \Delta t \dot{x}_{t-1} \quad (4)$$
$$\dot{x}_t = \dot{x}_{t-1} \quad (5)$$

The complete state vector $X \in \mathbb{R}^{10}$is defined as:

$$X = \left[x_c, y_c, O_w, O_h, \theta, \dot{x}_c, \dot{y}_c, \dot{O}_w, \dot{O}_h, \dot{\theta}\right]^T \quad (6)$$

Where x_c, y_c represent the centroid coordinates of the detected marker in the image frame. The filter states correspond to both the observed variables and their first-order derivatives. The dynamic model of the system is expressed as:

$$X_t = A_t X_{t-1} + w_t \quad (7)$$

With the transition matrix $A_t \in \mathbb{R}^{10\times10}$ given by:

$$A_t = \begin{bmatrix} I_{5\times5} & \Delta t I_{5\times5} \\ 0_{5\times5} & I_{5\times5} \end{bmatrix} \quad (8)$$

Where $w_t \sim \mathcal{N}(0, Q_t)$, and $Q_t \in \mathbb{R}^{10\times10}$is the covariance matrix of the process noise. Similarly, the measurement model of the filter is defined as:

$$Y_t = H_t X_t + v_t \quad (9)$$
$$\mathrm{H}_t = [\mathrm{I}_{5\times5},\ 0_{5\times5}] \quad (10)$$

Where $v_t \sim \mathcal{N}(0, R_t)$ and $R_t \in \mathbb{R}^{5\times5}$ is the covariance matrix of the observation noise. The prediction step of the Kalman filter is computed at each time step, regardless of whether new measurements are available:

$$\dot{x}_t = A_t \dot{x}_{t-1} \quad (11)$$
$$\mathrm{P}_t = A_t P_{t-1} A_t^T + Q_t \quad (12)$$

When the detection module obtains an observation, the correction process is performed using the following equations:

$$\mathrm{Y}_t = Z_t - H_t \dot{x}_t \quad (13)$$
$$S_t = H_t P_t H_t^T + R_t \quad (14)$$
$$K_t = P_t H_t^T S_t^{-1} \quad (15)$$
$$\dot{x}_t = \dot{x}_t + K_t Y_t \quad (16)$$
$$P_t = (I_{10\times10} - K_t H_t) P_t \quad (17)$$

The Kalman filter estimates the resulting states, which correspond to the fiducial marker's position and orientation in each image frame. These estimates then control the UAV's motion, ensuring the quadcopter maintains stable alignment during the autonomous landing maneuver. In the implementation, the Kalman Filter was configured to smooth fluctuations in centroid coordinates obtained from the visual detection process. This filtering step reduces positional noise and provides stable feedback for UAV alignment, contributing to the consistency of landing error measurements observed in the simulation results.

RESULTS AND DISCUSSION

Simulation Data Results

We analyzed the simulation data to evaluate the performance of five fiducial marker types based on four main parameters: X-axis error, Y-axis error, landing time, and marker detection distance. The virtual onboard camera used in the simulation was configured with a horizontal field of view (FOV) of 2.0 radians, an image resolution of 640×480 pixels, and an R8G8B8 (8-bit RGB) color format.

These parameters remained constant across all tests to ensure consistent detection conditions for all markers**.** We tested each parameter using one-way analysis of variance (One-Way ANOVA) to determine whether marker groups differed significantly. We then conducted a Tukey HSD follow-up test to identify marker pairs with statistically significant differences.

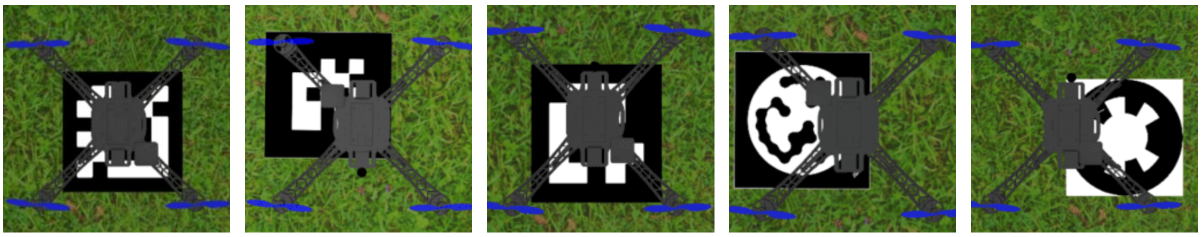

(a) (b) (c) (d) (e)

Figure 5. Sample UAV Quadcopter Simulation Results, (a) AprilTag, (b) ARTag, (c) ArUco, (d) STag, (e) WhyCode

All tests used a significance level of α = 0.05. Figure 5 shows the sample UAV quadcopter simulation results for different fiducial markers, illustrating the markers used during the evaluation.

X-Axis Error Analysis

Figure 6 presents raw simulation data for X-axis position error parameters for the five marker types tested, each in five tests under identical conditions.

Table 3 summarizes the mean values and variances. Based on these descriptive statistics, the mean X-axis error ranged from 2.994 cm to 7.280 cm, with the highest variance in STag. These differences in ranges indicate variation in performance between markers, which should be tested inferentially using analysis of variance (ANOVA).

Based on the ANOVA test results in Table 4, the F value = 1.04 with a p-value = 0.411 > 0.05 indicates that there is no significant difference between the average X-axis errors of the five marker types. Table 5 presents the parameters used in the Tukey HSD post-hoc test for X-axis error, with a Mean Squared Error (MSE) of 16.230482. The Tukey HSD test in Table 6 supports this, showing that no marker pairs differ significantly.

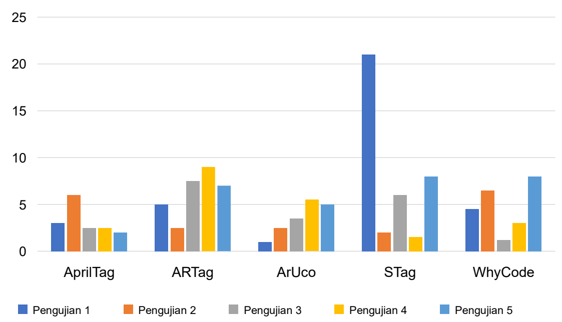

Figure 6. Comparative Data for X-Axis Error

Table 3. Descriptive Statistics X-Axis Error

Groups	Count	Sum	Average	Variance
AprilTag	5	14.97	2.994	2.04598
ARTag	5	29.42	5.884	5.63108
ArUco	5	15.89	3.178	4.08527
STag	5	36.40	7.280	61.5588
WhyCode	5	21.13	4.226	7.83128

Table 4. One-Way ANOVA for X-Axis Error

	SS	df	MS	F	P-value	F crit
Between Groups	67.54	4	16.88	1.04	0.41	2.86
Within Groups	324.60	20	16.23			
Total	392.15	24				

Table 5. Parameters for Tukey HSD Post Hoc Test for X-Axis

Parameter	Value
MSE	16.230482
n	5
k	5
df_within	20
q (α=0.05, k=5, df=20)	4.11

Table 6. Tukey HSD Post Hoc Test for X-Axis Error

Group1	Group2	MeanDiff	Significant
AprilTag	ARTag	2.890	No
AprilTag	ArUco	0.184	No
AprilTag	STag	4.286	No
AprilTag	WhyCode	1.232	No
ARTag	ArUco	2.706	No
ARTag	STag	1.396	No
ARTag	WhyCode	1.658	No
ArUco	STag	4.102	No
ArUco	WhyCode	1.048	No
STag	WhyCode	3.054	No

This confirms that all markers have comparable horizontal performance, and the small variation in mean values reflects minor inaccuracies in camera position estimation rather than algorithmic differences between markers.

Y-Axis Error Analysis

Figure 7 and Table 7 show the raw data results and descriptive statistics for the UAV's vertical position error relative to the marker. The average position error varied from 5.588 cm for AprilTag to 17.548 cm for ARTag. The highest variance was also found in ARTag, indicating a wide spread of data due to unstable marker detection.

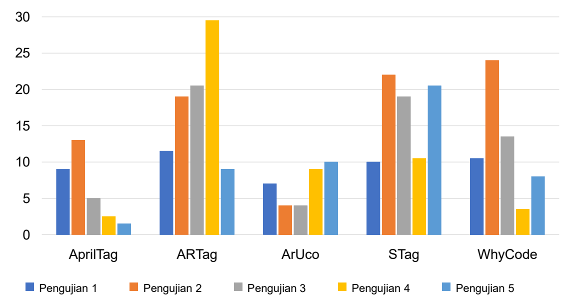

Figure 7. Comparative Data Y-Axis Error

Table 7. Descriptive Statistics Y-Axis Error

Groups	Count	Sum	Average	Variance
AprilTag	5	27.94	5.588	27.29372
ARTag	5	87.74	17.548	67.71737
ArUco	5	28.62	5.724	15.40923
STag	5	79.97	15.994	32.99888
WhyCode	5	57.16	11.432	60.44092

The considerable variation between these groups formed the basis for testing whether the differences were statistically significant through ANOVA.

Based on the ANOVA test results in Table 8, an F value of 3.82 with a p-value of 0.018 < 0.05 was obtained, indicating a significant difference between markers in Y-axis error. Table 9 presents the parameters used in the Tukey HSD post-hoc test for Y-axis error, with a MSE of 40.772024.

Meanwhile, the Tukey HSD post-hoc test in Table 10 shows significant differences between the AprilTag–ARTag and ARTag–ArUco pairs. Scientifically, this indicates that differences in marker pattern design affect the consistency of vertical position estimation. Thus, Y-axis differences are more sensitive to markers' geometric characteristics and visual contrast, while the detection algorithm's influence remains within statistically reasonable limits.

Landing Time Analysis

Figure 8 and Table 11 show the UAV's average landing time for each marker. The average values range from 15.8 s to 21.8 s with considerable variation in STag. The highest average for AprilTag suggests a higher detection computational load, which was further tested to determine whether differences between markers were significant.

Table 8. One-Way ANOVA for Y-Axis Error

Source of Variation	SS	df	MS	F	P-value	F crit
Between Groups	623.99	4	155.99	3.82	0.01	2.86
Within Groups	815.44	20	40.77			
Total	1439.43	24				

Table 9. Parameters for Tukey HSD Post Hoc Test for Y-Axis

Parameter	Value
MSE	40.772024
n	5
k	5
df_within	20
q (α=0.05, k=5, df=20)	4.11

Table 10. Tukey HSD Post Hoc Test for Y-Axis Error

Group1	Group2	MeanDiff	Significant
AprilTag	ARTag	11.96	Yes
AprilTag	ArUco	0.136	No
AprilTag	STag	10.406	No
AprilTag	WhyCode	5.844	No
ARTag	ArUco	11.824	Yes
ARTag	STag	1.554	No
ARTag	WhyCode	6.116	No
ArUco	STag	10.27	No
ArUco	WhyCode	5.708	No
STag	WhyCode	4.562	No

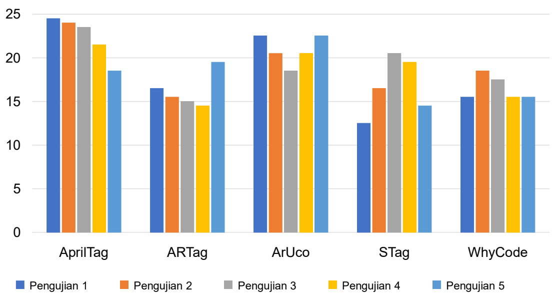

Figure 8. Comparative Data for Landing Time

Table 11. Descriptive Statistics Landing Time

Groups	Count	Sum	Average	Variance
AprilTag	5	109	21.8	5.7
ARTag	5	79	15.8	3.7
ArUco	5	102	20.4	2.8
STag	5	81	16.2	11.2
WhyCode	5	80	16.0	2.0

The ANOVA test results in Table 12 show an F value of 7.94 with a p-value of 0.000529 < 0.05, indicating a significant difference between markers. Table 13 presents the parameters used in the Tukey HSD post-hoc test for landing time, with a Mean Squared Error (MSE) of 5.08.

The Tukey HSD test results in Table 14 also show that significant differences occur between several pairs, particularly AprilTag–ARTag, AprilTag–STag, and AprilTag–WhyCode, as well as between ARTag–ArUco.

Table 12. One-Way ANOVA for Landing Time

Source of Variation	SS	df	MS	F	P-value	F crit
Between Groups	161.36	4	40.34	7.94	0.0005 29	2.86
Within Groups	101.6	20	5.08			
Total	262.96	24				

Table 13. Parameter to Tukey HSD Post Hoc Test for Landing Time

Parameter	Value
MSE	5.08
n	5
k	5
df_within	20
q (α=0.05, k=5, df=20)	4.11

Table 14. Tukey HSD Post Hoc Test for Landing Time

Group1	Group2	MeanDiff	Significant
AprilTag	ARTag	6.0	Yes
AprilTag	ArUco	1.4	No
AprilTag	STag	5.6	Yes
AprilTag	WhyCode	5.8	Yes
ARTag	ArUco	4.6	Yes
ARTag	STag	0.4	No
ARTag	WhyCode	0.2	No
ArUco	STag	4.2	Yes
ArUco	WhyCode	4.4	Yes
STag	WhyCode	0.2	No

This indicates that differences in code structure and marker detection complexity directly affect the visual system's speed in performing position corrections. Markers with simpler code designs and faster detection, such as ArUco and WhyCode, tend to produce shorter landing times. In contrast, markers with more complex identification computations take longer to reach stability. Thus, landing time is the most sensitive indicator of visual algorithm efficiency and shows a direct relationship between marker complexity and navigation system response.

Detected Marker Distance Analysis

Figure 9 and Table 15 show the maximum detection distance data for each marker. The average values range from 2.296 m for ARTag to 3.176 m for AprilTag, with relatively low variance for almost all markers. This distribution suggests that certain markers have better detection capabilities, so further testing is needed to confirm statistical significance.

Based on the ANOVA results in Table 16, the F value = 13.65 with a p-value = $1.59\times10^{-5} < 0.05$ indicates a significant difference between markers in detection distance. Table 17 presents the parameters used in the Tukey HSD post-hoc test for detected marker distance, with a Mean Squared Error (MSE) of 0.04.

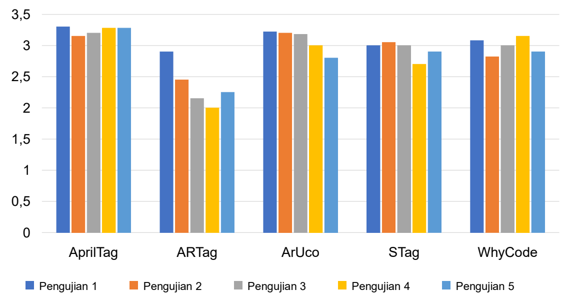

Figure 9. Comparative Data for Detected Marker Distance

Table 15. Descriptive Statistics Detected Marker Distance

Groups	Count	Sum	Average	Variance
AprilTag	5	15.88	3.176	0.00563
ARTag	5	11.48	2.296	0.12663
ArUco	5	15.15	3.030	0.0353
STag	5	14.37	2.874	0.01898
WhyCode	5	14.64	2.928	0.02022

Table 16. One-Way ANOVA for Detected Marker Distance

Source of Variation	SS	df	MS	F	P-value	F crit
Between Groups	2.25	4	0.56	13.65	1.59	2.86
Within Groups	0.82	20	0.04			
Total	3.08	24				

Table 17. Parameter to Tukey HSD Post Hoc Test for Detected Marker Distance

Parameter	Value
MSE	0.04
n	5
k	5
df_within	20
q (α=0.05, k=5, df=20)	4.11

The Tukey HSD results in Table 18 also indicate significant differences between AprilTag–ARTag, ARTag–ArUco, ARTag–STag, and ARTag–WhyCode. This confirms that detection distance is strongly influenced by marker-pattern complexity and contrast against the background. Markers with an optimal edge-to-fill ratio enable feature-based detection algorithms to work more efficiently in varying simulated lighting conditions. Statistically, the detection distance parameter is the main indicator that significantly differentiates marker performance, as it is directly related to image-capture effectiveness and the speed of visual feature identification.

Comparative Study

Based on the statistical results, the observed performance differences among fiducial markers are not only empirical but also explainable through visual signal-processing characteristics, marker geometry, and their interaction with homography-based pose estimation and closed-loop UAV control. AprilTag's superiority is therefore not merely numerical but structural, in terms of detection pipeline robustness and geometric conditioning.

Table 18. Tukey HSD Post Hoc Test for Detected Marker Distance

Group1	Group2	MeanDiff	Significant
AprilTag	ARTag	0.88	Yes
AprilTag	ArUco	0.146	No
AprilTag	STag	0.302	No
AprilTag	WhyCode	0.248	No
ARTag	ArUco	0.734	Yes
ARTag	STag	0.578	Yes
ARTag	WhyCode	0.632	Yes
ArUco	STag	0.156	No
ArUco	WhyCode	0.102	No
STag	WhyCode	0.054	No

From a visual signal-processing perspective, AprilTag is more robust because its detection pipeline emphasizes gradient-consistent edge extraction, quad segmentation, and probabilistic bit decoding with built-in error correction. The binary pattern maximizes inter-bit contrast and spatial-frequency separation, increasing signal-to-noise ratio (SNR) during thresholding and edge detection. In feature-based detection, higher edge contrast produces more stable corner responses and reduces descriptor ambiguity, leading to lower correspondence error during feature matching and homography estimation. Comparative experimental studies of fiducial markers consistently report that AprilTag yields lower false-positive rates and more stable pose estimates under noise and blur conditions compared to other square markers [25] [30].

Geometrically, marker layout directly affects homography stability because the projective transform matrix is estimated from corner correspondences. Homography conditioning depends on point distribution, angular separation, and edge orthogonality. Markers with strong square geometry, uniform border thickness, and sharp corners produce better-conditioned homography matrices with lower numerical sensitivity to pixel noise. AprilTag uses thick black–white borders and symmetric cell grids that preserve corner detectability under perspective distortion, thereby reducing reprojection residuals. Markers with more complex or less uniformly contrasted internal patterns tend to generate higher corner jitter, which propagates into centroid and pose variance. This explains why vertical (Y-axis) error shows statistically significant differences while X-axis error does not: vertical image coordinates are more sensitive to perspective scaling and projective skew during descent, so homography instability appears first along that axis.

Detection distance differences can also be explained through spatial-frequency response. Markers that maintain recognizable macro-geometry at lower pixel resolution can be detected earlier in the image pyramid. AprilTag's coding scheme preserves global quad structure even when inner bits are partially unresolved, allowing early-stage candidate validation. In contrast, markers whose decoding depends more heavily on internal fine patterns require higher pixel density for reliable identification. This behavior has been reported in cross-marker evaluations where AprilTag and STag maintain longer effective detection ranges than legacy ARTag variants under identical optics and resolution constraints [25] [26].

From a control-systems standpoint, pose-estimation noise directly affects the stability of the visual-servoing loop used in precision landing. The UAV landing controller continuously converts image-plane centroid error into lateral velocity or position corrections. If marker detection produces high-variance centroid estimates, the feedback loop experiences measurement noise that increases control oscillation and prolongs settling time. In the presented framework, the Kalman filter attenuates part of this noise, but filter performance is bounded by measurement covariance. Therefore, markers that intrinsically generate lower observation noise, such as AprilTag, lead to smoother innovation sequences, faster filter convergence, and more stable descent trajectories. This explains why AprilTag shows slightly longer average landing time yet lower vertical error. The controller performs smaller, more stable corrective actions instead of aggressive oscillatory corrections triggered by noisy measurements.

For real UAV deployment, these findings suggest aligning marker selection with control-loop sensitivity and mission risk rather than detection speed alone. In outdoor precision landing scenarios subject to motion blur, illumination variation, and camera vibration, markers with strong geometric primitives and error-correcting binary structure provide more reliable pose feedback and reduce the probability of control divergence near touchdown. Faster-detected markers with lighter decoding, such as ArUco or WhyCode, remain suitable for time-critical but lower-precision tasks; however, for safety-critical landing on constrained pads, markers with higher geometric and signal robustness offer superior operational margins. Prior UAV landing studies using multi-marker and redundancy strategies also support the conclusion that geometric stability and decoding robustness, rather than raw detection latency alone, are primary determinants of final landing accuracy.

CONCLUSION

This study presented a standardized simulation-based framework to comparatively evaluate five fiducial markers, AprilTag, ARTag, ArUco, STag, and WhyCode, for UAV precision landing using a unified PX4, ROS, and Gazebo environment. By enforcing identical marker dimensions, camera parameters, and lighting settings, the framework enabled controlled statistical comparison using homography-based pose estimation and Kalman-filtered visual observations.

The results show that marker geometry and coding structure significantly influence pose-estimation stability, particularly in the vertical axis, detection distance, and landing-time behavior. Markers with stronger geometric regularity and higher edge contrast produced more stable homography estimation and lower measurement variance, which in turn improved closed-loop landing stability. Within the tested simulation conditions, AprilTag consistently showed lower vertical error and longer detection distance, indicating stronger robustness in visual signal extraction and geometric conditioning than the other evaluated markers.

However, these findings must be interpreted within the limits of simulation-based experimentation. The reported performance reflects controlled virtual conditions and does not yet incorporate real-world disturbances such as illumination variability, motion blur, camera vibration, lens distortion, atmospheric effects, and onboard processing constraints. Therefore, the results support that AprilTag is the best-performing marker within the simulated and standardized test framework, rather than establishing it as universally optimal for all operational environments.

The primary contribution of this work is a statistically validated, reproducible comparative methodology that links marker design, visual geometry stability, and control-response behavior. Future work should extend this framework to hardware-in-the-loop and real-flight experiments, include varying marker scales and surface materials, and evaluate robustness under dynamic outdoor conditions. Such validation is necessary before generalizing marker-selection guidelines for safety-critical UAV precision-landing deployment.

ACKNOWLEDGMENT

The authors acknowledge the Ministry of Higher Education, Science, and Technology (Kemendiktisaintek) and Universitas Negeri Semarang (UNNES) for research funding number 48.20.6/UN37/PPK.10/2023 - 281.12.4/UN37/PPK.10/2023 and academic support that facilitated this study. We extend special appreciation to the Institute for Research and Community Service (LPPM) and the Faculty of Engineering for their institutional assistance. Furthermore, the authors sincerely thank the Artificial Intelligence, Robotics, and Internet of Things (AIRIoT) Laboratory at the Digital Center UNNES for providing the technical resources and laboratory facilities essential to this research.

REFERENCES

[1] B. Chen, “Research on AI Application in the Field of Quadcopter UAVs,” in *2020 IEEE 2nd International Conference on Civil Aviation Safety and Information Technology (ICCASIT*, 2020, pp. 569–571. doi: 10.1109/ICCASIT50869.2020.9368551.

[2] A. Marut, P. Wojciechowski, K. Wojtowicz, and K. Falkowski, “Visual-based landing system of a multirotor UAV in GNSS denied environment,” in *2023 IEEE 10th International Workshop on Metrology for AeroSpace (MetroAeroSpace)*, 2023, pp. 308–313. doi: 10.1109/MetroAeroSpace57412.2023.10190013.

[3] S. A. Akbar, M. T. D. Akbar, A. Yudhana, and K. H. Ghazali, “Vision-guided tracking and detection using the YOLOv5 model on a logistic delivery fixed-wing UAV,” *Sinergi (Indonesia)*, vol. 30, no. 2, pp. 449–458, Jun. 2026, doi: 10.22441/sinergi.2026.2.011.

[4] J.-S. Liu and H.-C. Liu, “Visual Navigation for UAVs Landing on Accessory Building Floor,” in *2020 International Conference on Pervasive Artificial Intelligence (ICPAI)*, 2020, pp. 158–163. doi: 10.1109/ICPAI51961.2020.00037.

[5] J. Wang, D. McKiver, S. Pandit, A. F. Abdelzaher, J. Washington, and W. Chen, “Precision UAV Landing Control Based on Visual Detection,” in *2020 IEEE Conference on Multimedia Information Processing and Retrieval (MIPR)*, 2020, pp. 205–208. doi: 10.1109/MIPR49039.2020.00049.

[6] J. C. Welgemoed, R. L. Phillips, and T. I. van Niekerk, “An Autonomous Multirotor UAV for Security Systems in Rural South Africa,” in *2023 14th International Conference on Mechanical and Intelligent Manufacturing Technologies (ICMIMT)*, 2023, pp. 12–18. doi: 10.1109/ICMIMT59138.2023.10200559.

[7] G. Badakis, M. Koutsoubelias, and S. Lalis, “Robust Precision Landing for Autonomous Drones Combining Vision-based and Infrared Sensors,” in *2021 IEEE Sensors Applications Symposium (SAS)*, 2021, pp. 1–6. doi: 10.1109/SAS51076.2021.9530091.

[8] P. R. Grobler and H. W. Jordaan, “Autonomous Vision Based Landing Strategy for a Rotary Wing UAV,” in *2020 International SAUPEC/RobMech/PRASA Conference*, 2020, pp. 1–6. doi: 10.1109/SAUPEC/RobMech/PRASA48453.2020.9041238.

[9] K. Kishore *et al.*, "3D Pure Pursuit Guidance of Drones for Autonomous Precision Landing," in *2022 13th Asian Control Conference (ASCC)*, 2022, pp. 2218–2222. doi: 10.23919/ASCC56756.2022.9828198.

[10] A. S. Nair, P. A. Jeyanthy, L. Ramesh, G. M. Kurian, and S. R. Mohamed, "Autonomous Precision Landing with UAV and Auto charging," in *2021 International Conference on Recent Trends on Electronics, Information, Communication & Technology (RTEICT)*, 2021, pp. 463–466. doi: 10.1109/RTEICT52294.2021.9573947.

[11] L. Xia and J. Li, "Autonomous Landing of a Fixed-Wing UAV With RTK GNSS and MEMS IMU," *International Journal of Aerospace Engineering*, vol. 2025, no. 1, p. 9430096, Jan. 2025, doi: 10.1155/ijae/9430096.

[12] D. Ekaso, F. Nex, and N. Kerle, "Accuracy assessment of real-time kinematics (RTK) measurements on unmanned aerial vehicles (UAV) for direct geo-referencing," *Geo-spatial Information Science*, vol. 23, no. 2, pp. 165–181, Apr. 2020, doi: 10.1080/10095020.2019.1710437.

[13] L. Yang, J. Ye, Y. Zhang, L. Wang, and C. Qiu, "A semantic SLAM-based method for navigation and landing of UAVs in indoor environments," *Knowl. Based. Syst.*, vol. 293, p. 111693, 2024, doi: 10.1016/j.knosys.2024.111693.

[14] T.-T. Nguyen *et al.*, "Visual-based localization methods for unmanned aerial vehicles in landing operation on maritime vessel," *Acta IMEKO*, vol. 13, no. 4, pp. 10–13, 2024, doi: 10.21014/actaimeko.v13i4.1575.

[15] C. Wang, J. Wang, C. Wei, Y. Zhu, D. Yin, and J. Li, "Vision-Based Deep Reinforcement Learning of UAV-UGV Collaborative Landing Policy Using Automatic Curriculum," *Drones*, vol. 7, no. 11, Nov. 2023, doi: 10.3390/drones7110676.

[16] N. Ma, X. Weng, Y. Cao, and L. Wu, "Monocular-Vision-Based Precise Runway Detection Applied to State Estimation for Carrier-Based UAV Landing," *Sensors*, vol. 22, no. 21, Nov. 2022, doi: 10.3390/s22218385.

[17] Y. Park *et al.*, "Fiducial Marker-Based Autonomous Landing Using Image Filter and Kalman Filter," *International Journal of Aeronautical and Space Sciences*, vol. 25, no. 1, pp. 190–199, 2024, doi: 10.1007/s42405-023-00635-y.

[18] N. T. Sanjukumar, A. V. V Meghashyam, Bhuvanesh, and P. Rajalakshmi, "TDMBPLD: A Dataset Focusing on Marker Scene for UAV Landing," *IEEE Geoscience and Remote Sensing Letters*, vol. 22, pp. 1–5, 2025, doi: 10.1109/LGRS.2025.3567863.

[19] M. Kilin, R. Lavrenov, Y. Bai, M. Svinin, and E. Magid, "Testing Procedures Architecture for Establishing a Fiducial Marker Recognition Quality in UAV-based Visual Marker Tracking Task in Gazebo Simulator," 2022. [Online]. Available: http://robot.kpfu.ru/eng

[20] V. R. F. Miranda, A. M. C. Rezende, T. L. Rocha, H. Azpúrua, L. C. A. Pimenta, and G. M. Freitas, "Autonomous Navigation System for a Delivery Drone," *Journal of Control, Automation and Electrical Systems*, vol. 33, no. 1, pp. 141–155, Feb. 2022, doi: 10.1007/s40313-021-00828-4.

[21] J. Saunders, S. Saeedi, and W. Li, "Autonomous aerial robotics for package delivery: A technical review," *J. Field Robot.*, vol. 41, no. 1, pp. 3–49, Jan. 2024, doi: 10.1002/rob.22231.

[22] T. Cui, C. Guo, Y. Liu, and Z. Tian, "Precise Landing Control of UAV Based on Binocular Visual SLAM," in *2021 4th International Conference on Intelligent Autonomous Systems (ICoIAS)*, 2021, pp. 312–317. doi: 10.1109/ICoIAS53694.2021.00062.

[23] B. Li, J. Wu, X. Tan, and B. Wang, "ArUco Marker Detection under Occlusion Using Convolutional Neural Network," in *2020 5th International Conference on Automation, Control and Robotics Engineering (CACRE)*, 2020, pp. 706–711. doi: 10.1109/CACRE50138.2020.9230250.

[24] H. D. Tran *et al.*, "A Multiple Marker Design for Precision and Redundant Visual Landing in Drone Delivery," in *2023 12th International Conference on Control, Automation and Information Sciences (ICCAIS)*, 2023, pp. 127–132. doi: 10.1109/ICCAIS59597.2023.10382271.

[25] M. Kalaitzakis, B. Cain, S. Carroll, A. Ambrosi, C. Whitehead, and N. Vitzilaios, "Fiducial Markers for Pose Estimation: Overview, Applications and Experimental Comparison of the ARTag, AprilTag, ArUco and STag Markers," *J. Intell. Robot. Syst.*, vol. 101, May 2021, doi: 10.1007/s10846-020-01307-9.

[26] J. Ulrich, A. Alsayed, F. Arvin, and T. Krajn\'{\i}k, “Towards fast fiducial marker with full 6 DOF pose estimation,” in *Proceedings of the 37th ACM/SIGAPP Symposium on Applied Computing*, in SAC ’22. New York, NY, USA: Association for Computing Machinery, 2022, pp. 723–730. doi: 10.1145/3477314.3507043.

[27] M. Kalaitzakis, S. Carroll, A. Ambrosi, C. Whitehead, and N. Vitzilaios, “Experimental Comparison of Fiducial Markers for Pose Estimation,” in *2020 International Conference on Unmanned Aircraft Systems (ICUAS)*, 2020, pp. 781–789. doi: 10.1109/ICUAS48674.2020.9213977.

[28] R. M. Claro, F. S. P. Neves, and A. M. G. Pinto, “A Multimodal Perception System for Precise Landing of UAVs in Offshore Environments,” *J. Field Robot.*, vol. 42, no. 5, pp. 2151–2172, Aug. 2025, doi: https://doi.org/10.1002/rob.22517.

[29] M. Bertoni, S. Michieletto, R. Oboe, and G. Michieletto, “Indoor Visual-Based Localization System for Multi-Rotor UAVs,” *Sensors*, vol. 22, no. 15, Aug. 2022, doi: 10.3390/s22155798.

[30] D. Jurado-Rodriguez, R. Muñoz-Salinas, S. Garrido-Jurado, and R. Medina-Carnicer, “Planar fiducial markers: a comparative study,” *Virtual Real.*, vol. 27, no. 3, pp. 1733–1749, 2023, doi: 10.1007/s10055-023-00772-5.

[31] M. Kalaitzakis, B. Cain, S. Carroll, A. Ambrosi, C. Whitehead, and N. Vitzilaios, “Fiducial Markers for Pose Estimation,” *J. Intell. Robot. Syst.*, vol. 101, no. 4, p. 71, 2021, doi: 10.1007/s10846-020-01307-9.

[32] K. T. Putra, H. Zidni, M. Y. Mustar, D. F. Alfiansyah, R. A. Ghifari, and M. S. B. A. Talip, “Computer Vision-Driven Precision Landing in Quadcopter Drones Using ArUco Markers,” in *2024 4th International Conference on Electronic and Electrical Engineering and Intelligent System (ICE3IS)*, 2024, pp. 236–240. doi: 10.1109/ICE3IS62977.2024.10775518.

[33] R. I. Naufal, N. Karna, and S. Y. Shin, “Vision-based Autonomous Landing System for Quadcopter Drone Using OpenMV,” in *2022 13th International Conference on Information and Communication Technology Convergence (ICTC)*, 2022, pp. 1233–1237. doi: 10.1109/ICTC55196.2022.9952383.

[34] A. Annusewicz and J. Zwierzchowski, “Marker Detection Algorithm for the Navigation of a Mobile Robot,” in *2020 27th International Conference on Mixed Design of Integrated Circuits and System (MIXDES)*, 2020, pp. 223–226. doi: 10.23919/MIXDES49814.2020.9155658.

[35] Y. Huang, T. Zhang, T. Wu, and L. Yu, “Multi-AGV Coordination System Design with STag Marker,” in *2024 9th Asia-Pacific Conference on Intelligent Robot Systems (ACIRS)*, 2024, pp. 50–54. doi: 10.1109/ACIRS62330.2024.10684899.

[36] J. Springer and M. Kyas, “Autonomous Drone Landing with Fiducial Markers and a Gimbal-Mounted Camera for Active Tracking,” in *2022 Sixth IEEE International Conference on Robotic Computing (IRC)*, 2022, pp. 243–247. doi: 10.1109/IRC55401.2022.00047.

[37] J. Wubben *et al.*, “Accurate Landing of Unmanned Aerial Vehicles Using Ground Pattern Recognition,” *Electronics (Basel).*, vol. 8, no. 12, 2019, doi: 10.3390/electronics8121532.

[38] K. Dang Nguyen and T.-T. Nguyen, “Vision-Based Software-in-the-Loop-Simulation for Unmanned Aerial Vehicles Using Gazebo and PX4 Open Source,” in *2019 International Conference on System Science and Engineering (ICSSE)*, 2019, pp. 429–432. doi: 10.1109/ICSSE.2019.8823322.

[39] M. A. Kasno, N. M. Yatim, T.-W. Kang, J. M. Hee, J. Nam, and J.-W. Jung, “Voice-Controlled Navigation for TurtleBot3 using ROS Noetic and Speech Recognition,” in *2024 15th International Conference on Information and Communication Technology Convergence (ICTC)*, 2024, pp. 1970–1971. doi: 10.1109/ICTC62082.2024.10826802.

[40] N. Lilansa, M. N. Rizal, P. Anggraeni, and J. Ramadhan, “Implementation consensus algorithm and leader-follower of multi-robot system formation,” *SINERGI*, vol. 27, no. 1, pp. 45–56, 2023, doi: 10.22441/sinergi.2023.1.006

[41] K. T. T. Moyo, J. V. S. Luces, A. A. Ravankar, Y. Hirata, and M. Shota, “Enhancing Manipulator Flexibility: Real-time Positional Control for Variable Assembly Environments using AprilTag Markers and Edge Detection,” in *2024 IEEE 20th International Conference on Automation Science and Engineering (CASE)*, 2024, pp. 3932–3939. doi: 10.1109/CASE59546.2024.10711707.

[42] X. Blake, K. Sathirakul, and N. Aphiratsakun, "Location, orientation, and speed tracking of a robot using ROS: a case study with Whycon," in *2023 International Electrical Engineering Congress (iEECON)*, 2023, pp. 377–380. doi: 10.1109/iEECON56657.2023.10126552.

[43] M. Saavedra-Ruiz, A. M. Pinto-Vargas, and V. Romero-Cano, "Monocular Visual Autonomous Landing System for Quadcopter Drones Using Software in the Loop," *IEEE Aerospace and Electronic Systems Magazine*, vol. 37, no. 5, pp. 2–16, 2022, doi: 10.1109/MAES.2021.3115208.